LISA Pathfinder platform stability and drag-free performance

M. Armano,[1] H. Audley,[2] J. Baird,[3] P. Binetruy,[3,*] M. Born,[2] D. Bortoluzzi,[4] E. Castelli,[5] A. Cavalleri,[6] A. Cesarini,[7] A. M. Cruise,[8] K. Danzmann,[2] M. de Deus Silva,[9] I. Diepholz,[2] G. Dixon,[8] R. Dolesi,[5] L. Ferraioli,[10] V. Ferroni,[5] E. D. Fitzsimons,[11] M. Freschi,[9] L. Gesa,[12] F. Gibert,[5] D. Giardini,[10] R. Giusteri,[5] C. Grimani,[7] J. Grzymisch,[1] I. Harrison,[13] G. Heinzel,[2] M. Hewitson,[2] D. Hollington,[14] D. Hoyland,[8] M. Hueller,[5] H. Inchauspé,[3,15,‡] O. Jennrich,[1] P. Jetzer,[16] N. Karnesis,[3] B. Kaune,[2] N. Korsakova,[17] C. J. Killow,[17] J. A. Lobo,[12,†] I. Lloro,[12] L. Liu,[5] J. P. López-Zaragoza,[12] R. Maarschalkerweerd,[13] D. Mance,[10] N. Meshksar,[10] V. Martín,[12] L. Martin-Polo,[9] J. Martino,[3] F. Martin-Porqueras,[9] I. Mateos,[12] P. W. McNamara,[1] J. Mendes,[13] L. Mendes,[9] M. Nofrarias,[12] S. Paczkowski,[2] M. Perreur-Lloyd,[17] A. Petiteau,[3] P. Pivato,[5] E. Plagnol,[3] J. Ramos-Castro,[18] J. Reiche,[2] D. I. Robertson,[17] F. Rivas,[12] G. Russano,[5] J. Slutsky,[19] C. F. Sopuerta,[12] T. Sumner,[14] D. Texier,[9] J. I. Thorpe,[19] D. Vetrugno,[5] S. Vitale,[5] G. Wanner,[2] H. Ward,[17] P. J. Wass,[14,15] W. J. Weber,[5] L. Wissel,[2] A. Wittchen,[2] and P. Zweifel[10]

(LISA Pathfinder Collaboration)

[1]*European Space Technology Centre, European Space Agency, Keplerlaan 1, 2200 AG Noordwijk, The Netherlands*
[2]*Albert-Einstein-Institut, Max-Planck-Institut für Gravitationsphysik und Leibniz Universität Hannover, Callinstraße 38, 30167 Hannover, Germany*
[3]*APC, Univ Paris Diderot, CNRS/IN2P3, CEA/lrfu, Obs de Paris, Sorbonne Paris Cité, France*
[4]*Department of Industrial Engineering, University of Trento, via Sommarive 9, 38123 Trento, and Trento Institute for Fundamental Physics and Application/INFN*
[5]*Dipartimento di Fisica, Università di Trento and Trento Institute for Fundamental Physics and Application/INFN, 38123 Povo, Trento, Italy*
[6]*Istituto di Fotonica e Nanotecnologie, CNR-Fondazione Bruno Kessler, I-38123 Povo, Trento, Italy*
[7]*DISPEA, Università di Urbino "Carlo Bo", Via S. Chiara, 27 61029 Urbino/INFN, Italy*
[8]*The School of Physics and Astronomy, University of Birmingham, Birmingham, United Kingdom*
[9]*European Space Astronomy Centre, European Space Agency, Villanueva de la Cañada, 28692 Madrid, Spain*
[10]*Institut für Geophysik, ETH Zürich, Sonneggstrasse 5, CH-8092, Zürich, Switzerland*
[11]*The UK Astronomy Technology Centre, Royal Observatory, Edinburgh, Blackford Hill, Edinburgh, EH9 3HJ, United Kingdom*
[12]*Institut de Ciències de l'Espai (CSIC-IEEC), Campus UAB, Carrer de Can Magrans s/n, 08193 Cerdanyola del Vallès, Spain*
[13]*European Space Operations Centre, European Space Agency, 64293 Darmstadt, Germany*
[14]*High Energy Physics Group, Physics Department, Imperial College London, Blackett Laboratory, Prince Consort Road, London, SW7 2BW, United Kingdom*
[15]*Department of Mechanical and Aerospace Engineering, MAE-A, P.O. Box 116250, University of Florida, Gainesville, Florida 32611, USA*
[16]*Physik Institut, Universität Zürich, Winterthurerstrasse 190, CH-8057 Zürich, Switzerland*
[17]*SUPA, Institute for Gravitational Research, School of Physics and Astronomy, University of Glasgow, Glasgow, G12 8QQ, United Kingdom*
[18]*Department d'Enginyeria Electrònica, Universitat Politècnica de Catalunya, 08034 Barcelona, Spain*
[19]*Gravitational Astrophysics Lab, NASA Goddard Space Flight Center, 8800 Greenbelt Road, Greenbelt, Maryland 20771, USA*

(Received 14 December 2018; published 16 April 2019; corrected 5 November 2019)

The science operations of the LISA Pathfinder mission have demonstrated the feasibility of sub-femto-g free fall of macroscopic test masses necessary to build a gravitational wave observatory in space such as LISA. While the main focus of interest, i.e., the optical axis or the x-axis, has been extensively studied, it is also of great importance to evaluate the stability of the spacecraft with respect to all the other degrees of

[*]Deceased March 30, 2017.
[†]Deceased September 30, 2012.
[‡]hinchauspe@ufl.edu

freedom (d.o.f.). The current paper is dedicated to such a study: the exhaustive and quantitative evaluation of the imperfections and dynamical effects that impact the stability with respect to its local geodesic. A model of the complete closed-loop system provides a comprehensive understanding of each component of the in-loop coordinates spectral density. As will be presented, this model gives very good agreement with LISA Pathfinder flight data. It allows one to identify the noise source at the origin and the physical phenomena underlying the couplings. From this, the stability performance of the spacecraft with respect to its geodesic is extracted as a function of frequency. Close to 1 mHz, the stability of the spacecraft on the X_{SC}, Y_{SC} and Z_{SC} d.o.f. is shown to be of the order of 5.0×10^{-15} m s^{-2} Hz$^{-1/2}$ for X, 6.0×10^{-14} m s^{-2} Hz$^{-1/2}$ for Y, and 4.0×10^{-14} m s^{-2} Hz$^{-1/2}$ for Z. For the angular d.o.f., the values are of the order of 3×10^{-12} rad s^{-2} Hz$^{-1/2}$ for Θ_{SC}, 5×10^{-13} rad s^{-2} Hz$^{-1/2}$ for H_{SC}, and 3×10^{-13} rad s^{-2} Hz$^{-1/2}$ for Φ_{SC}. Below 1 mHz, however, the stability performances are worsened significantly by the effect of the star tracker noise on the closed-loop system. It is worth noting that LISA is expected to be spared from such concerns, as differential wave-front sensing, an attitude sensor system of much higher precision, will be utilized for attitude control.

DOI: 10.1103/PhysRevD.99.082001

I. GENERAL INTRODUCTION

The stability of a space platform, described by the low noise acceleration of the platform with respect to the local geodesic, is a quality that is often desired in order to satisfy the requirements of scientific observations or to perform tests of fundamental physics. Examples of such activities range from high precision geodesy, gravity field, and gradient measurements (GRACE [1], GOCE [2]); experimental tests of gravitation (GPB [3], MICROSCOPE [4]); gravitational wave astronomy [LISA Pathfinder (LPF), the Laser Interferometer Space Antenna (LISA)]; or astrometry missions such as Gaia [5] requiring attitude stability of the order of a few nrad s^{-1} [6]. Using two quasi-free-falling test masses (TMs), LPF [7] has demonstrated remarkable properties related to its stability, and recent publications (see [8] and [9]) have presented the observed performance of the differential mode (TMs relative stability) along the axis joining the two test masses. However, the importance of the stability of the LPF platform is not limited to the differential mode and to this axis; therefore, in this paper we present results associated to the six degrees of freedom (d.o.f.) of the spacecraft (S/C). In order to evaluate this performance, it is necessary not only to make use of the internal measurement of its sensors and actuators but also to deduce the *true* motion of the spacecraft (S/C) impacted by the imperfections of the sensor and actuator systems. It is also required to evaluate the relative motion between the test masses and the platform due to in-loop forces whose manifestation is hidden from most sensors because the closed-loop control scheme nulls the measurement of in-loop sensors on LPF. In this paper we first introduce the configuration of the LPF platform and then the closed-loop control scheme that allows the observed performance to be achieved. In order to understand how this performance is reached, we introduce a simplified, linear, time invariant state-space model (SSM) which allows extrapolation from in-loop sensor outputs in order to obtain needed physical quantities otherwise unobserved. An important example of such a quantity is the actual low-frequency relative displacement between the test masses and the S/C, driven by the sensor noise and masked by the closed-loop system (see further details in Sec. VII). We show that this model is capable of reproducing the observations of the sensors to within a few percent and can therefore be relied upon. The last section, before the conclusion, is devoted to summing up all the effects that allow the stability of LPF with respect to its local geodesic over the six d.o.f. to be deduced.

II. THE LISA PATHFINDER PLATFORM

LPF [10] aims to demonstrate that it is technically possible to make inertial reference frames in space at the precision required by low-frequency gravitational wave astronomy. Indeed, in a space-based observatory design such as LISA [11], one needs excellent references of inertia inside each satellite in order to differentiate between spurious accelerations of the apparatus from gravitational radiation, which both result in detected oscillatory variation of the arm lengths of the spacecraft constellation. The quality of free fall achieved along the X-axis, the axis of main interest (i.e., representing axes along LISA arms), has already significantly exceeded expectations [8]. In addition to limiting stray forces acting directly on the TM, the LPF differential acceleration result required stringent and specific control of the TM-S/C relative motion, to limit elastic "stiffness" coupling and possible cross-talk effects. Besides, postprocessing software corrections from modeling of such S/C-to-test mass acceleration couplings have been proven to be necessary and efficient in order to extract measurements of residual acceleration exerted on the TMs only (such as inertial forces, stiffness coupling, and cross-talk corrections [8]).

The control scheme required challenging technologies permitting high precision sensing and actuation in order to

finely track and act on the three bodies and keep them at their working point. The LISA Technology Package (LTP), the main payload of LPF, was built to demonstrate the feasibility of the targeted sensitivity [10] and includes high performance sensing and actuation subsystems. The gravitational reference sensor (GRS) [12] includes the 1.93 kg Au-Pt test mass, surrounded by a conducting electrostatic shield with electrodes that are used for simultaneous capacitive position sensing and electrostatic force actuation of the TM [13,14]. The optical metrology system (OMS) [15–17] uses heterodyne interferometry for high precision test mass displacement measurements. Angular displacements are sensed through the differential wavefront sensing (DWS) using phase differences measured across the four quadrants of photodiodes. The star tracker (ST) orients the spacecraft with respect to a Galilean frame and the micropropulsion system, a set of six cold gas thrusters (a technology already flown in space with ESA's Gaia mission [5] and CNES's MICROSCOPE mission [4]), allows S/C displacement and attitude control along its six d.o.f. Note that LPF also has a NASA participation, the Space Technology 7 (ST7) mission, contributing a set of eight colloidal thrusters and the electronics/computer that control them [18].

III. THE DRAG-FREE AND ATTITUDE CONTROL SYSTEM (DFACS)

The drag-free and attitude control system (DFACS) [19] is a central subsystem in LPF architecture. It has been designed by Airbus Defence & Space [20]. It is devoted to achieving the control scheme that maintains the test masses to be free falling at the center of their electrode housings (translation control), to keep a precise alignment of the TMs with respect to the housing inner surfaces (rotation control) and to track the desired spacecraft orientation with respect to inertial frames (spacecraft attitude control). The translational control strategy is designed to limit any applied electrostatic suspension forces on the TMs to the minimum necessary to compensate any differential acceleration between the two TMs, while the common-mode motion of these geodesic references, which essentially reflects S/C accelerations, is drag-free controlled with the microthrusters [21]. Limiting the applied actuation forces limits a critical acceleration noise from the actuator gain noise. This drag-free control is essentially used to counterbalance the noisy motion of the spacecraft, which is exposed both to the space environment and to its own thrust noise. A linear combination of test mass coordinates inside their housing along the Y- and Z-axes is preferred for drag-free control, translational thrust being used to correct common-mode displacements while rotational actuations are performed to correct differential-mode displacements (see Table I, entries 5–8). Due to the geometrical configuration of the experiment (see Fig. 1), differential x-displacements of the TMs cannot be corrected by the drag-free control. In this case, it is necessary to apply control forces on one of the TMs along the X-axis. The strategy used is to leave TM1 in pure free fall while the second mass is forced to follow the first, in order to keep the relative position of the masses constant at low frequencies. The amount of electrostatic force required to achieve this is measured and accounted for in the computation of the acceleration noise experienced by the masses [8]. This control scheme is called "suspension control." All the angular coordinates of the test masses (except rotation around x_1) are controlled by the suspension control scheme (see Table I). The attitude of the spacecraft with respect to Galilean frame is supported by the attitude

TABLE I. Control scheme of LISA Pathfinder in nominal science mode. For each system's dynamical coordinate, the table lists by which subsystem it is sensed, its associated control type and the actuator used. d is the distance between the TMs.

Number	Coordinates	Sensor system	Control mode	Actuation system
1	Θ	ST	Attitude	GRS (Tx_1)
2	H	ST	Attitude	GRS ($Fz_2 - Fz_1$)
3	Φ	ST	Attitude	GRS ($Fy_2 - Fy_1$)
4	x_1	IFO	Drag-free	μ-thrust ($\uparrow$ X-axis)
5	$\frac{y_2+y_1}{2}$	GRS	Drag-free	μ-thrust ($\uparrow$ Y-axis)
6	$\frac{z_2+z_1}{2}$	GRS	Drag-free	μ-thrust ($\uparrow$ Z-axis)
7	$\frac{y_2-y_1}{d}$	GRS	Drag-free	μ-thrust ($\circlearrowleft$ Z-axis)
8	$\frac{z_2-z_1}{d}$	GRS	Drag-free	μ-thrust ($\circlearrowleft$ Y-axis)
9	θ_1	GRS	Drag-free	μ-thrust ($\circlearrowleft$ X-axis)
10	x_{12}	IFO	Suspension	GRS (Fx_2)
11	η_1	IFO	Suspension	GRS (Ty_1)
12	ϕ_1	IFO	Suspension	GRS (Tz_1)
13	θ_2	GRS	Suspension	GRS (Tx_2)
14	η_2	IFO	Suspension	GRS (Ty_2)
15	ϕ_2	IFO	Suspension	GRS (Tz_2)

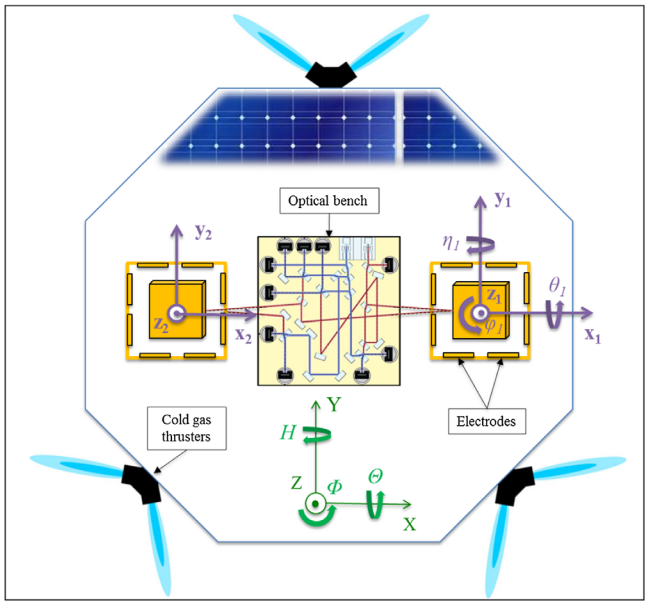

FIG. 1. Simplified sketch of LISA Pathfinder apparatus. The system of coordinates used to describe the displacement of the test masses (purple sets of axes) and of the spacecraft (green set of axes) is made explicit.

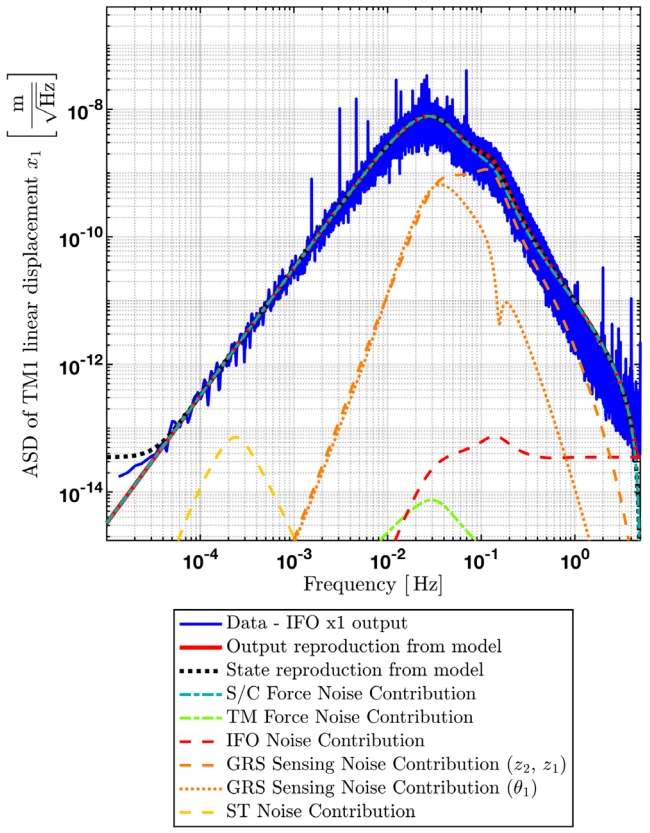

FIG. 2. Decomposition of the spectral density of the in-loop interferometer (IFO) measurement along x_1 (also called o_1 in the text, for optical x_1), giving the linear motion of TM1 along x, into the various contributions from the sensing noises and the external disturbances. The solid blue curve corresponds to the LPF data. The red curve is built from modeled closed-loop transfer functions (SSM) with noise level from Table II. The other curves give the individual contributions of the most relevant noise channels. This plot is assuming a GRS z sensing with a noise floor of 1.8×10^{-9} m $\mathrm{Hz}^{1/2}$ and a $1/f$ noise increase from 1 mHz and below. The S/C force and torque noise levels, extracted from Eq. (4), are all measured to be consistent with white noise. The white noise level along the X-axis is measured to be of 0.17 $\mu\mathrm{N}\,\mathrm{Hz}^{-1/2}$. See Sec. VI and Table II for more details.

control. Because the commanded torques on the satellite are driven by the drag-free control of the differential linear displacement of the masses along the Y- and Z-axes, as previously mentioned, the attitude control is realized indirectly. First, the attitude control demands differential forces on the masses according to information coming from the star trackers. Then, the drag-free loop corrects the induced differential displacement by requiring a rotation of the spacecraft, thus executing the rotation imposed by the star trackers.

IV. STEADY-STATE PERFORMANCE: A FREQUENCY DOMAIN ANALYSIS

This study focuses on the LPF data during the measurement campaign where very long noise-only runs were operated in nominal science mode [22]: data collected in April 2016 and January 2017 are considered here. The "noise-only run" designation means that the closed loop is left to operate freely without injecting any excitation signal of any kind. The 15 in-loop measurements, listed in Table I, are studied in the frequency domain. As in-loop measurements, they do not strictly reflect the dynamical state (i.e., the true displacements) of the TMs inside their housings, but represent the error signal of the control loop for each measurement channel, the working point being zero for all the d.o.f. except for the S/C attitude. The week-long data sets sampled at 10 Hz are processed through Welch's modified periodogram method [23,24] to estimate variance-reduced power spectral densities of the measurement outputs, using fifteen 50% overlapping Blackmann-Harris windowed average segments.

As an example, Fig. 2 shows the spectral density of the o_1 channel during the April 2016 run, i.e., the in-loop optical sensor readout of the x_1 coordinate (cf. reference axes of Fig. 1). In the figure are traced together the observed data (in solid blue) and the sum of all the contributors (in red), as predicted by a SSM of the closed-loop system [25] [cf. Sec. V and Eq. (2)]. The remaining lines show the breakdown of the different components that contribute significantly to the sum: the external, out-of-loop forces applied on the S/C and the GRS sensing noise (mostly z_1 and z_2 sensing noise as visible after breaking down the contribution further) which are superimposed.

The S/C force noise curve (turquoise) is due to the microthruster noise, for movements along X and rotation around Y. This has been demonstrated by comparing the colloidal and cold gas micronewton thruster systems independently and jointly [18]. Note that the presence of a strong GRS sensing noise component, around 0.1 Hz, is due to the control strategy. Further details about this model reconstruction, and other examples, are given in Sec. V.

The residual spectrum of o_1 reflects the frequency behavior of the drag-free control gain. Below 0.1 Hz, the control-loop gain is high and counters the noisy forces applied on the S/C (mostly thruster noise but also solar noise, etc.). The drag-free gains continuously decrease with increasing frequencies to reach a minimum around 30 mHz. The spectrum is conversely increasing as f^2, reaching its maximum jitter level of about 7 nm $\mathrm{Hz}^{-1/2}$ around 30 mHz. At higher frequencies, the $1/f^2$ behavior, due to the inertia of the TMs, is responsible for the spectrum drop. On the right of the plot, above 1 Hz, one would normally see the readout noise floor only. At a high enough frequency, the system is almost insensitive to any external stray forces applied on the S/C, thus causing no significant S/C-to-TMs displacements, because of the $1/f^2$ behavior of the dynamics which filters out high-frequency excitation. Hence, above 1 Hz, it is safe to consider that the signals observed by most of the in-loop sensors are dominated by sensing noise, except for IFO x_1 measurements however, as shown by the red dashed line on the right of the plot. Indeed, the optical sensing noise is outstandingly low, less than 0.1 pm $\mathrm{Hz}^{-1/2}$ as already presented in [8], such that displacements continue to be resolvable even above 1 Hz. Figure 2 shows that IFO sensing noise has no perceptible impact on in-loop o_1 in the whole frequency range of interest. The discrepancy between the data (solid blue line) and the model prediction (solid red line) visible above 0.5 Hz is considered to be due to the imperfection of the SSM model which does not reflect the nonlinear nature of the micronewton thruster system (e.g., pure delays). This has been confirmed by a comparison with the European Space Agency (ESA) end-to-end simulator that does not assume this linear aspect.

The spectrum breakdown also gives interesting information about the multiple-input-multiple-output (MIMO) nature of the in-loop dynamics. In Fig. 2, this appears clearly with the superimposed orange dashed lines that show the influence of the GRS sensing noise on the spectrum of x_1, yet sensed by the OMS. Indeed, z_1 and z_2 sensing noise induces noisy S/C Y-axis (η) rotations as expected from the control scheme outlined in Table I. This motion causes an apparent x-axis displacement of TM1 inside its housing, and the projection depends on the geometrical position of the housing with respect to the center of mass of the S/C. This effect competes with force noise on the S/C at high frequencies.

V. SPECTRUM DECOMPOSITION USING A STATE-SPACE MODEL OF THE SYSTEM

As shown in the previous section, breaking down the data according to a physical model turns out to be very informative for tracking down the physical origins of the spectral behavior of the in-loop coordinates. This model developed by the LPF Collaboration [25] (and implemented within the LTPDA software [26]) is a linear, time invariant state-space model, meaning that the modeled dynamical behavior of the closed-loop system does not depend on time or on the dynamical state. The latter is encoded within a state-space representation in such a way that the Nth-order differential system governing the dynamics transforms into a matrix system of N first-order equations, thus benefiting from the matrix algebra arsenal. The linearity and stationarity of the model allows for straightforward conversions between time-domain SSM and frequency domain transfer functions. The superposition principle holds because of linearity and allows one to decompose all the resulting spectral densities into their various contributions by extracting the relevant single-input-single-output (SISO) transfer functions from the MIMO model. In that spirit, the in-loop sensor outputs can be decomposed with the help of closed-loop transfer functions called "sensitivity functions," which encode the sensitivity of the outputs to various out-of-loop disturbance signals, such as the sensing noise or the force noise applied on the bodies. Their respective transfer functions are named the sensitivity function (S-gain) and the load disturbance sensitivity function (L-gain) as typically seen in the literature. They are given by the following expressions:

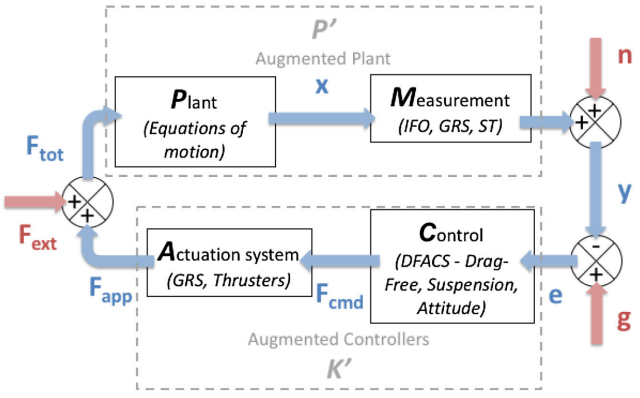

FIG. 3. Simplified diagram of the LPF closed-loop system. The closed-loop system is excited via three different out-of-loop signal channels: the guidance signal g (null in the case of a noise-only run), the sensing noise n, and the external forces F_{ext}. The in-loop variables are indicated in blue, whereas the out-of-loop signals are in red. The in-loop variables are successively the states of motion X, the observed displacements Y, the error signal compared to targeted displacements e, the commanded F_{cmd} forces, the effectively applied forces F_{app}, and the total resulting forces F_{tot}.

$$S(f) = \frac{1}{1 + P'K'} \quad L(f) = \frac{P'}{1 + P'K'}$$
$$T(f) = \frac{P'K'}{1 + P'K'}, \tag{1}$$

whereas P, standing for "plant," is the transfer functions of the dynamical system under DFACS control (forces/torques to displacements) and K encodes the transfer functions of the DFACS. The prime symbols denote that these transfer functions also include the transfer functions of the actuators ($K' = KA$) and of the sensors ($P' = MP$), for the sake of notation simplification. Hence, these closed-loop transfer functions potentially depend on all the subsystem transfer functions involved in the control loop and, more significantly, on the plant dynamics and the control laws. Figure 3 gives an illustration of the LPF closed-loop system which shows explicitly these transfer functions and the various in-loop and out-of-loop variables. Mathematically, the spectrum breakdown can be expressed in the following way:

$$\tilde{Y}^q = \sum_{p=x,y,z,\theta,\eta,\phi} L^{qp}_{\text{gain}} \tilde{F}^p_{\text{ext}} + \sum_{p=x,y,z,\theta,\eta,\phi} S^{qp}_{\text{gain}} \tilde{n}^p, \tag{2}$$

where $\tilde{Y}^q$, $\tilde{F}^p_{\text{ext}}$, and $\tilde{n}^p$ are the Fourier transforms, for the d.o.f. q, of the associated in-loop sensor output, the out-of-loop force noises and sensing noises [27], respectively. Because the S-gain and the L-gain are both MIMO functions, a sum is performed over the extra dimension

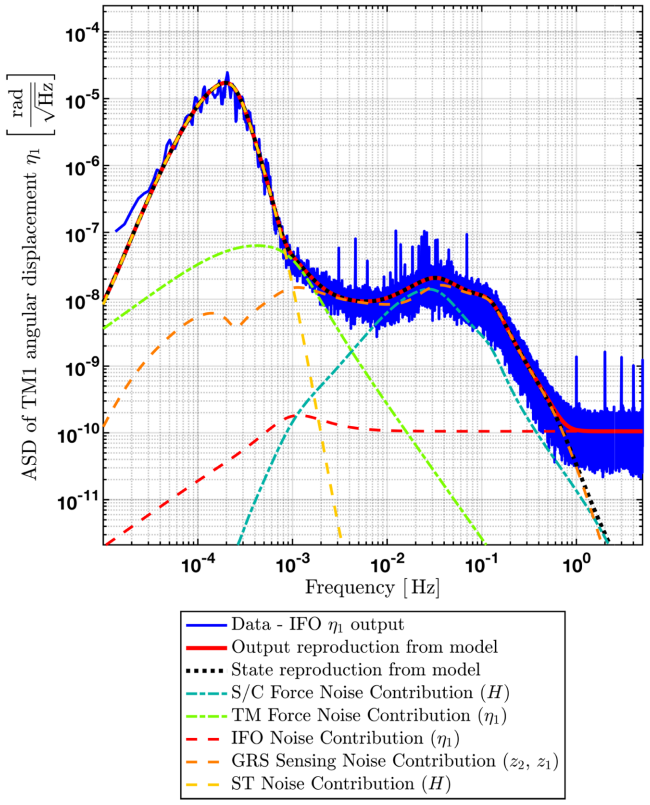

FIG. 4. Decomposition of the in-loop DWS measurement η_1 spectrum into its various noise source contributions. The same explanations as in Fig. 2 apply. In this plot, we assume a ST sensing noise of 3.7×10^{-4} rad $\text{Hz}^{-1/2}$ at 0.2 mHz, with a noise floor starting from 5 mHz at a level of 2.0×10^{-5} rad $\text{Hz}^{-1/2}$; a TM torque noise of 7.1×10^{-16} N $\text{Hz}^{-1/2}$ across the whole bandwidth; a GRS z sensing with a noise floor of 1.8×10^{-9} m $\text{Hz}^{1/2}$; a $1/f$ noise increase from 1 mHz and below, reaching a level of 4.6×10^{-9} m $\text{Hz}^{1/2}$ at 0.1 mHz; a S/C torque noise around its Y-axis of 6.7×10^{-8} N m $\text{Hz}^{-1/2}$; a white DWS η noise of 1.05×10^{-10} rad $\text{Hz}^{-1/2}$. See Sec. VI and Table II for more details.

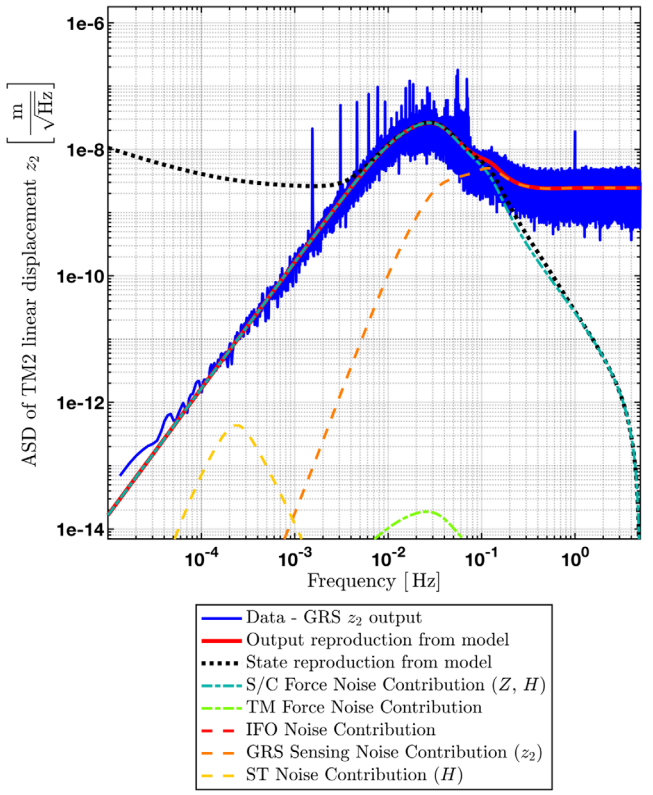

FIG. 5. Decomposition of the in-loop GRS measurement z_2 spectrum into its various noise source contributions. The same explanations as in Fig. 2 apply. Note that the z_2 state (black dashed line)—or z_2 "true motion"—predicted from the model deviates very significantly from the in-loop GRS sensed z_2 displacement (data in solid blue, model in solid red). As discussed in detail in Sec. VII, the GRS sensor noise induces jitters of the S/C at low frequency (here $f < 1$ mHz) which is not observable from the in-loop GRS z_2 output. In this plot, we assume a GRs z sensing with a noise floor of 1.5×10^{-9} m $\text{Hz}^{1/2}$ and a $1/f$ noise increase from 1 mHz and below, reaching a level of 4.5×10^{-9} m $\text{Hz}^{1/2}$ at 0.1 mHz. The S/C force and torque noise levels, extracted from Eq. (4), are all measured to be consistent with white noise. The white noise level along the Z-axis is measured to be of 4.6×10^{-7} N $\text{Hz}^{-1/2}$. See Sec. VI and Table II for more details.

TABLE II. Table of sensing and actuation noises. N.S. stands for "not sensitive" and W.N. stands for "white noise." See the text for further explanations.

Number	Sensing noise	April 2016	January 2017	f_c:α	Actuation noise	April 2016	January 2017	f_c:α
1	o_1(m Hz$^{-1/2}$)	35.0×10^{-15}	N.S.	N.S.	Ext. X(N Hz$^{-1/2}$)	1.7×10^{-7}	1.9×10^{-7}	W.N.
2	y_1(m Hz$^{-1/2}$)	1.5×10^{-9}	1.5×10^{-9}	1 mHz:−0.5	Ext. Y(N Hz$^{-1/2}$)	1.4×10^{-7}	1.7×10^{-7}	W.N.
3	z_1(m Hz$^{-1/2}$)	1.8×10^{-9}	1.7×10^{-9}	1 mHz:−0.5	Ext. Z(N Hz$^{-1/2}$)	4.6×10^{-7}	3.3×10^{-7}	W.N.
4	θ_1(rad Hz$^{-1/2}$)	9.4×10^{-8}	1.1×10^{-7}	1 mHz:−0.5	Ext. θ(N m Hz$^{-1/2}$)	9.8×10^{-8}	7.5×10^{-8}	W.N.
5	η_1(rad Hz$^{-1/2}$)	1.05×10^{-10}	1.06×10^{-10}	1 mHz:−0.5	Ext. η(N m Hz$^{-1/2}$)	6.7×10^{-8}	7.8×10^{-8}	W.N.
6	ϕ_1(rad Hz$^{-1/2}$)	2.05×10^{-10}	2.05×10^{-10}	1 mHz:−0.5	Ext. ϕ(N m Hz$^{-1/2}$)	1.7×10^{-7}	1.9×10^{-7}	W.N.
7	ST θ(rad Hz$^{-1/2}$)	2.1×10^{-6}	2.1×10^{-6}	See text	Fy_1(N Hz$^{-1/2}$)	8.0×10^{-15}		1 mHz:−1
8	ST η(rad Hz$^{-1/2}$)	2.0×10^{-5}	2.0×10^{-5}	See text	Fz_1(N Hz$^{-1/2}$)	8.0×10^{-15}		1 mHz:−1
9	ST ϕ(rad Hz$^{-1/2}$)	3.2×10^{-6}	3.2×10^{-6}	See text	Ty_1(N m Hz$^{-1/2}$)	7.1×10^{-16}	7.4×10^{-16}	W.N.
10					Tz_1(N m Hz$^{-1/2}$)	2.6×10^{-16}	1.9×10^{-16}	W.N.

to account for cross-coupling effects that can have an important impact on the spectra (like the role played by GRS sensing noise in the spectra of Fig. 2).

A number of instances illustrate this type of decomposition. A case of particular interest is the spectra of the TMs' angular displacements around the y and z axes, corresponding to the angles labeled η and ϕ [28]. The residuals behave in the most complex fashion because of numerous contributions competing to alter the TM orientation. As an example, Fig. 4 shows the spectral density of the in-loop η_1 optical sensing output. Every control type of the DFACS—drag-free, suspension, and attitude controls—has an influence on this plot.

At the highest frequencies, the η_1 DWS sensing noise (dashed red line) is the dominant factor. From 0.5 mHz to 0.5 Hz there is a complex interplay among the external forces applied on the S/C (i.e., micronewton thrusters, turquoise dashed line); residuals of the drag-free compensation; and the GRS sensing noise (orange dashed line) of z_1, z_2, and θ_1 that are all drag-free controlled. At the lowest frequencies, the star tracker noise (yellow) which acts through the attitude control is the dominant source. It should be noted that some of these noise sources, such as the GRS z_1 and z_2 sensing noise (orange), can be measured more directly through other channels; for example, see the analysis done in Fig. 5. In the region around 1 mHz in Fig. 4, one is in the presence of an ambiguity because the observed spectrum can either be explained by the impact of the TM torque noise of η_1 (light green) or by enhancing the reddening of the noise of the z_1 and z_2 sensors. To remove this ambiguity, the reddening ($1/f$ behavior) has been measured independently in [13].

Figure 5 shows the behavior of the z_2 sensing output. This case is representative of what can also be observed for drag-free variables such as outputs y_1, y_2, z_2, and θ_1. These spectra are much simpler than for the η and ϕ channels. At the highest frequencies, the sensing noise (of z_2 in the figure) can be directly extracted. At lower frequencies, the behavior of the spectra is essentially controlled by the Z external forces exerted on the S/C, which means an estimation of this noise is also readily measurable.

VI. SENSING AND ACTUATION NOISE

In the above section, Eq. (2) shows how the out-of-loop force and sensing noises impact the observed spectra. In this section we begin by giving some illustrative examples of how the noise levels impact different frequency ranges and we then present our quantitative results in Table II. Depending on the frequency range, a given noise will dominate the observed spectra. For instance, at the highest frequencies (typically from $f > 1$ Hz), observed displacements of the S/C and the TMs are nearly insensitive to input external forces. Indeed, referring to Eq. (2), $S_{\text{gain}} \approx 1$ and $L_{\text{gain}} \approx 0$ in such a region, reflecting the fact that the inertia of the bodies increases along with frequency, as a consequence of the $1/f^2$ behavior of the dynamical system (double integrator, i.e., from force to displacement). Consequently, the noise of a given sensor dominates the observed spectra in most cases, allowing for a straightforward determination of its level; see the red or orange dashed lines, respectively, in Fig. 4 or 5 as examples. An exception is shown in Fig. 2 where the sensor noise level is so low that even at the highest frequencies the sensitivity to the sensing noise is not reached and a determination of its noise level cannot be made. In Ref. [9], the x_1 IFO noise level is indeed shown to be as small as 30 fm Hz$^{-1/2}$. At lower frequencies, below 5 mHz, the out-of-loop S/C force noise usually dominates; see in Fig. 5 the dashed turquoise line. The level of these noises can be determined with the help of the commanded forces or torques on/around the corresponding axis [see Eq. (3), discussed later in the section]. In the case of Fig. 4 the situation is different and below 1 mHz the ST noise dominates (yellow dashed line). We discuss later in this section how these noises are estimated.

In most instances, the frequency dependence of the noises are not directly measurable by an analysis of the spectra, because they are here indistinguishable from that of the closed-loop model transfer function. We used

therefore the results of independent and dedicated investigations that were performed during the mission. For the capacitive sensing noises, we refer to [13] which showed that these noises had a $1/\sqrt{f}$ (in amplitude) dependence below 1 mHz, whereas, for the capacitive actuation noises, [14] showed a $1/f$ dependence (in amplitude) below 1 mHz. We have performed an analysis of all the observables (x, y, z, θ, η, and ϕ) associated to TM1 for a number of noise-only runs. The results, obtained for April 2016 and January 2017, are collected in Table II. In the left side (columns 2-5) of this table we list the sensing noises that we have used (see Table I for more details about the d.o.f.). The first six lines correspond to the linear and angular sensing noises of TM1, whereas the last three lines correspond to the S/C star tracker noise. The third and fourth columns give the values obtained in April 2016 and January 2017. The right side (columns 6-9) of the table gives the values for the actuation noises. The first six lines correspond to the out-of-loop forces and torques on the S/C, whereas the last five lines correspond to the capacitive actuation forces on TM1. The values given in this table correspond to the noise level at high frequencies. The fifth and ninth columns give the corner frequency and the spectral index of the reddening of the noise below the corner frequency, when applicable.

Two special cases have to be highlighted. The last three observables in the left side of the table (ST noise, entries 7–9) are obtained from a fit to the spectrum of the attitude control error signals out of the DFACS, corrected by the S-gain of the corresponding control loop. The attitude control is effective at frequencies well below the measurement bandwidth and the star tracker noise level dominates any actual S/C rotations in the latter bandwidth, which means that the attitude control error signal provides a direct measurement of the attitude sensor noise essentially, as confirmed by the state-space model of the closed-loop system. From these time series, a fit is obtained assuming a white noise at high frequencies, a rise for frequencies below 3 mHz, and a saturation below 0.4 mHz. The values given in Table II correspond to the white noise floor. It should be noted that the ST noise also shows a number of features, i.e., peaks in the frequency domain around 5 mHz, which are not included in the corresponding fits. With regards to the actuation noise in the right-hand side of the table, the first six entries correspond to the noisy external forces and torques applied on the S/C, essentially by the thruster system itself (as discussed in Sec. IV). This force noise can be measured from the calculation of the out-of-loop forces exerted on the S/C. Equations (3)–(5) present such calculations as follows:

$$\vec{n}^{\text{thruster}} \approx \begin{bmatrix} \vec{F}_{\text{SC}}^{\text{ool}} \\ \vec{T}_{\text{SC}}^{\text{ool}} \end{bmatrix} \tag{3}$$

$$\vec{F}_{\text{SC}}^{\text{ool}} = m_{\text{SC}} \begin{bmatrix} \ddot{o}_1 \\ \frac{\ddot{z}_1+\ddot{z}_2}{2} \\ \frac{\ddot{y}_1+\ddot{y}_2}{2} \end{bmatrix} - \vec{F}_{\text{SC}}^{\text{cmd}} \tag{4}$$

$$\vec{T}_{\text{SC}}^{\text{ool}} = I_{\text{SC}} \begin{bmatrix} \ddot{\theta}_1 - \frac{T_{x1}}{I_{1,xx}} \\ \frac{\ddot{z}_2-\ddot{z}_1}{2d} - \left(\frac{F_{z2}}{m_2} - \frac{F_{z1}}{m_1}\right) \\ \frac{\ddot{y}_1-\ddot{y}_2}{2d} - \left(\frac{F_{y1}}{m_1} - \frac{F_{y2}}{m_2}\right) \end{bmatrix} - \vec{T}_{\text{SC}}^{\text{cmd}}, \tag{5}$$

where the indices ool and cmd distinguish between out-of-loop forces and torques applied, and those commanded by the control loop (that oppose the ool forces and torques when the control gain is high). The meanings of the variables have been detailed in Table I. The mass terms m_{SC}, m_1, m_2, I_{SC}, and I_1 are the mass and the inertia matrices of the S/C and of the two TMs, respectively (the TMs are labeled by their numbers only). Also, d denotes the distance between the working points of the two TMs (namely, the centers of their housings).

The actuation noises of the capacitive actuators are addressed in the last five entries (7–11) on the right-hand side of the table. The force noise for the linear d.o.f. (y and z) is estimated from extrapolation of the x noise. It is built from the addition of the Brownian noise level observed for the x channels [8] and a model-based extrapolation of the actuation noise for d.o.f. other than x, which is expected to be dominant below 0.5 mHz because of the larger force and torque authorities along/around these axes. Regarding the torque noises (entries 9–10), their levels are measured at low frequency with the help of the following expression:

$$\vec{T}_{1/2}^{\text{ool}} = \frac{I_{1/2}}{\sqrt{2}} \begin{bmatrix} - \\ (\ddot{\eta}_2 - \ddot{\eta}_1) - \left(\frac{T_{y2}}{I_{2,yy}} - \frac{T_{y1}}{I_{1,yy}}\right) \\ (\ddot{\phi}_2 - \ddot{\phi}_1) - \left(\frac{T_{z2}}{I_{2,zz}} - \frac{T_{z1}}{I_{1,zz}}\right) \end{bmatrix}. \tag{6}$$

In Eq. (6), calculating the difference between IFO angular displacement measurements of the two TMs rejects common mode noise angular accelerations of the TMs and therefore the impact of the relative angular acceleration between the S/C and the TMs. Subtracting the capacitive commanded torques provides then an estimate of the out-of-loop torques on the TMs. However, this calculation is typically valid only below 1 mHz, above which frequency sensing noise rapidly dominates. Below 1 mHz, applying (6) to the data, a flat noise torque is observed down to around 0.01 mHz. As a conservative assumption, this white noise torque is averaged and extrapolated to the whole frequency band (hence labeled as white noise in Table II). Note that Eq. (6) is not applicable to linear d.o.f. y and z, since their differential channels are essentially sensitive to

the largely dominant S/C angular acceleration noise and are drag-free controlled. A similar limitation applies to the θ case [hence, the X-component of the torque vector is left blank in Eq. (6)].

In Table II, comparison between April 2016 and January 2017 data sets allows us to appreciate the consistency between the "noise runs" and the time invariance of the sensor and actuator performances. It is worth mentioning that the independent study in [18] also showed consistent results and similar performances for the cold-gas thrusters at different times of the mission (September 2016 and April 2017).

VII. THE STABILITY OF THE SPACECRAFT

It has been shown in the previous sections that the SSM was able to reproduce and explain the in-loop observations of the linear and angular displacements of the TMs relative to the S/C by breaking down the control residuals into the respective contributions of the individual noise sources. This model can now be used to assess physical quantities that are out of reach of the on-board sensors, such as "true displacement" of the bodies and their acceleration with respect to their local inertial frame.

Using properties of the space state model, one can extract the true movement of the S/C with respect to the TMs. This is done using the following formula:

$$\tilde{\mathbf{X}}^{q}_{\mathrm{SC}} = \sum_{p=x,y,z,\theta,\eta,\phi} L^{qp}_{\mathrm{gain}} \tilde{F}^{p}_{\mathrm{ext}} + \sum_{p=x,y,z,\theta,\eta,\phi} T^{qp}_{\mathrm{gain}} \tilde{n}^{p}, \quad (7)$$

where $\tilde{\mathbf{X}}^{q}_{\mathrm{SC}}$ is the Fourier transform, for the d.o.f. q, of the associated state variable, or alternatively called the true displacement (i.e., not the observed displacement) of the TMs with respect to the S/C. T^{qp}_{gain} is commonly named the T-gain or the complementary sensitivity function [27]. The difference between the true displacement and the observed displacement is that the former is estimated without applying the sensing noise, whereas the latter corresponds to the response of the sensor output, i.e., with its noise. It should be noted, however, that the noise of previous time steps has an impact on the true displacement.

This important distinction is a classical feature of in-loop variables of feedback systems. A closed-loop system will force the variable of interest to its assigned guidance value, generally zero. To do this, for example, it will apply a correcting force to the S/C that will not only compensate for any external disturbances, but will also be triggered by the noise of the corresponding position sensor, indistinguishable from the true motion from the point of view of the DFACS. As a result, when the sensing noise is the leading component, the compensating force will make the S/C jitter in the aim of canceling out the observed sensing noise. Hence, the state variable will exhibit this movement, whereas the sensor will show a value tending to its guidance at low frequency. Figure 8, discussed further in the text, illustrates this for the Z-axis acceleration.

Assuming TM1 follows a perfect geodesic, and following LPF's DFACS philosophy (see Table I), the stability of the S/C is defined by the dynamic variables shown in Eq. (8):

$$\begin{aligned} \ddot{X}_{\mathrm{SC}} &= \ddot{x}_1 \quad \ddot{\Theta}_{\mathrm{SC}} = \ddot{\theta}_1 \\ \ddot{Y}_{\mathrm{SC}} &= \frac{\ddot{y}_1 + \ddot{y}_2}{2} \quad \ddot{H}_{\mathrm{SC}} = \frac{\ddot{z}_2 - \ddot{z}_1}{d} \\ \ddot{Z}_{\mathrm{SC}} &= \frac{\ddot{z}_1 + \ddot{z}_2}{2} \quad \ddot{\Phi}_{\mathrm{SC}} = \frac{\ddot{y}_2 - \ddot{y}_1}{d}, \end{aligned} \quad (8)$$

where d is the distance between the two TMs.

However, the TMs cannot embody perfect local inertial frames, as they inevitably experience some stray forces, though of very low amplitude as previously demonstrated in [8]. Hence, as a second step, it is necessary to draw an estimation of the TMs' acceleration with respect to their local inertial frames and add it up to the relative acceleration between the TMs and the S/C calculated in the previous step. Reference [8] provides the acceleration noise floor due to Brownian noise ($S_0^{1/2} = 5.6\ \mathrm{fm\,s^{-2}\,Hz^{-1/2}}$, divided by $\sqrt{2}$ for the acceleration of a single TM), to which is added, in accordance with [9], a $1/f$ component starting from around 0.5 mHz and below.

Another factor that impacts the LPF stability is the GRS actuation noise. On the X-axis, the impact is minimal because the actuation authority is set to a minimal value, just above the one required to compensate for the internal gravity gradient. On the other axes and on the angular d.o.f. however, the actuation noise is expected to be dominant below 1 mHz according to model extrapolations for higher authority d.o.f. [14] (see Table II and discussion in Sec. VI).

Figures 6 and 7 present the stability (jitter) of the S/C and give a quantitative estimate of the true movement of the S/C (for linear and angular d.o.f., respectively) relative to the local geodesic. Figure 6 shows that the stability performance achieved by LPF for the translation d.o.f. platform reaches down to about $5.0 \times 10^{-15}\ \mathrm{m\,s^{-2}\,Hz^{-1/2}}$ for X, $6.0 \times 10^{-14}\ \mathrm{m\,s^{-2}\,Hz^{-1/2}}$ for Y, and $4.0 \times 10^{-14}\ \mathrm{m\,s^{-2}\,Hz^{-1/2}}$ for Z at best, at frequencies of around $f = 1$ mHz. For the angular d.o.f. treated in Fig. 7, the best achieved stability attains about $3 \times 10^{-12}\ \mathrm{rad\,s^{-2}\,Hz^{-1/2}}$ for Θ, $5 \times 10^{-13}\ \mathrm{rad\,s^{-2}\,Hz^{-1/2}}$ for H, and $3 \times 10^{-13}\ \mathrm{rad\,s^{-2}\,Hz^{-1/2}}$ for Φ, again at frequencies close to $f = 1$ mHz. The stability improves as frequency decreases, and in fact, as the drag-free control authority strengthens. However, below 1 mHz, the stability performances are worsened significantly by the effect of the star tracker noise on the closed-loop system. A detailed decomposition of this stability will be discussed in Sec. VIII.

It is worth noting that according to Fig. 7, H and Φ stabilities are better that the one observed for θ, between $1\ \mathrm{mHz} \leq f \leq 0.1$ Hz. This is because θ is measured by the electrodes of the single TM1, whereas η and ϕ are obtained

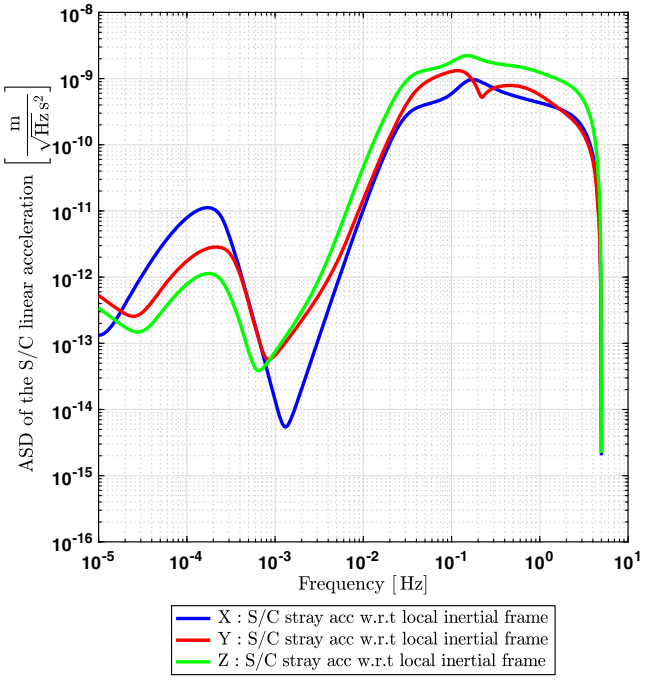

FIG. 6. Stability of the S/C along X, Y, and Z and as a function of frequency as simulated by the LPF state-space model using the parameters obtained from the April 2016 noise-only run.

from measurements using the two GRSs (combinations of z_1 and z_2 and of y_1 and y_2; see Table I), which leads to better signal-to-noise ratio benefiting from a larger lever arm between electrodes.

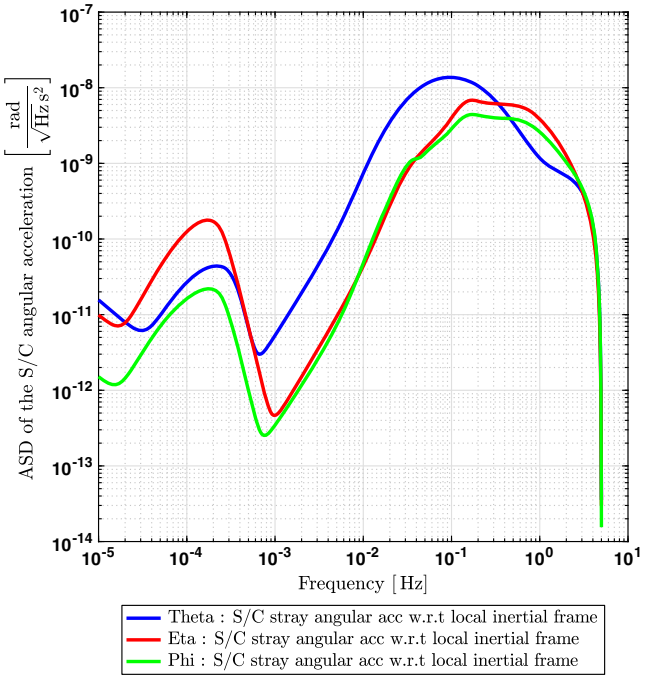

FIG. 7. Stability of the S/C along θ, η, and ϕ and as a function of frequency as simulated by the LPF state-space model using the parameters obtained from the April 2016 noise-only run.

VIII. DECOMPOSING THE STABILITY OF THE SPACECRAFT

Figures 6 and 7 present the stability of the S/C on all d.o.f. They show the complex behavior of this stability performance. It is important to understand where the observed features come from. As an example, Fig. 8 illustrates the decomposition of the acceleration stability on the Z-axis. Note that the Z stability for LPF is calculated as the average z values of TM1 and of TM2 [see Eq. (8)]. The red curve shows the sum of the listed contributions predicted by the SSM.

At the highest frequencies ($f > 0.5$ Hz) the Z sensing noise and the out-of-loop noise (i.e., mainly thruster noises) are predominant contributors. They are, however, countered by the inertia of the heavy S/C that does not allow it to move significantly, hence the roll-off of the red curve up to the Nyquist frequency at $f = 5$ Hz for these data. At lower frequencies (5 mHz $< f <$ 0.5 Hz), the out-of-loop forces are attenuated by the control loops, hence the exponential decrease below 10 mHz. Between 0.5 and 5 mHz, the GRS sensing noise on Z is the dominant factor. This creates a movement of the S/C because the closed-loop system erroneously interprets this sensing noise as a nonzero position of the TMs to be corrected by the displacement of the S/C. Below this range the ST noise dominates, while

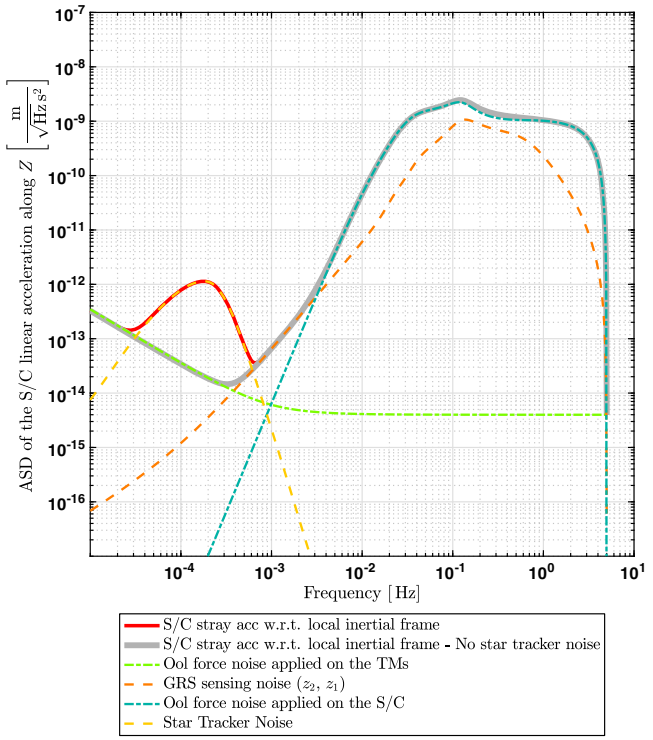

FIG. 8. Decomposition of the stability of the S/C along the Z-axis as a function of frequency. The red line shows the SSM prediction, and the other lines present each contribution to this model. The main contributors are the TM force noise (light green dashed line), the ST noise (orange dashed line), the GRS sensing noise (orange dashed lines), and the microthruster noise (turquoise dashed line). See the text for further explanation.

at the lowest frequencies, the capacitive actuation noise governs the platform stability.

These explanations can be applied to all d.o.f. with some differences for the X-axis. For this axis, the optical sensing noise is much smaller than GRS sensing noise and thus does not impact significantly the frequencies between 0.5 and 5 mHz. Another difference relates to the noise of capacitive actuation which is also much lower on X. At the lowest frequencies (around 0.01 mHz), one observes the impact of the $1/f$ "excess noise" discussed in [9].

IX. THE IMPACT OF THE STAR TRACKER NOISE

Most of the contributions to S/C acceleration with respect to the local inertial observer are readily understandable. However, the impact of the star tracker noise is more subtle and needs explanation. The reason it impacts the platform stability is because the center of mass of the S/C does not coincide with the midpoint between the TM housing positions. Eq. (9) defines the position of the center of each housing w.r.t. the center of mass of the S/C. By construction the center of mass is situated 62.5 mm below the housings along the Z-axis, but due to mechanical imperfections, it is also offset by a few millimeters on the X- and Y-axis [see Eq. (9) and Fig. 9].

$$\overrightarrow{BH_1} = \begin{bmatrix} 0.183 \\ -0.006 \\ 0.0625 \end{bmatrix} \text{m} \qquad \overrightarrow{BH_2} = \begin{bmatrix} -0.193 \\ -0.006 \\ 0.0625 \end{bmatrix} \text{m}. \quad (9)$$

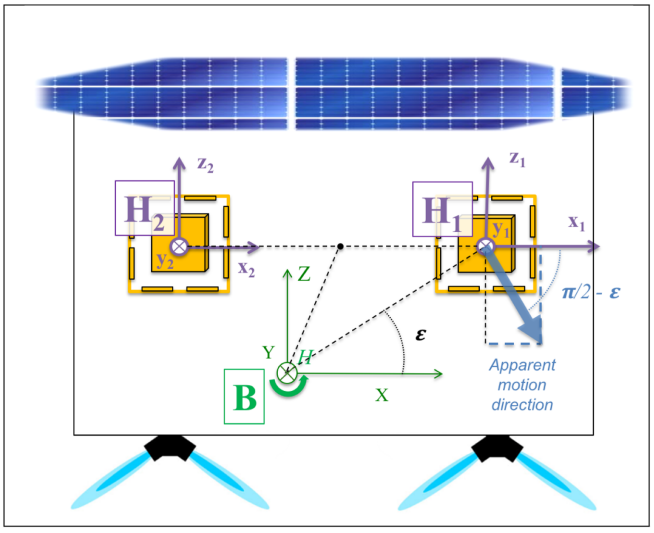

FIG. 9. Simplified sketch of the LPF apparatus. The xBz cross section is represented here. The figure shows how any rotation of the S/C, in particular an H-rotation around the Y-axis, leads to apparent displacement of TM1 inside its housing that has a significant component along the X-axis (proportional to $\sin\epsilon$ here) when the S/C center of mass is shifted from the center of the two housings.

Because of this, S/C rotation jitter driven by the noisy star tracker sensor induces an apparent linear displacement of the TMs inside their housings. Such linear displacement has a significant component along X if the center of mass happens to be offset with respect to the middle of the line joining the two TMs. The projection of the force on X indeed scales with the sine of the angle ϵ made by the line joining the center of the housing and the S/C center of mass (that is to say, the vector $B\vec{H}_1$), and the axis joining the two housings (the vector $H_1\vec{H}_2$). Such an effect can more formally be interpreted as the result of the (so-called) Euler force, an inertial force proportional to S/C angular acceleration arising from the point of view of a noninertial platform. Consequently, the drag-free control will react on and correct the (so-induced) displacement of TM1 inside its housing. What was only an apparent force applied on the test mass then becomes a true force applied on the S/C along X through the micronewton thrusters and the feedback control. In fact, everything happens as though there existed a rotation-to-translation coupling of the S/C displacement, due to S/C geometry and DFACS activity. It is also worth noting that the impact on X-axis stability is observed to be greatly reduced in the case where the center of mass lies in the line joining TM housing centers.

Equation (10) provides an expression for the inertial forces responsible for the TMs' displacement and Eq. (11) shows the drag-free control forces commanded to the micropropulsion system in order to correct for the effect of the inertial forces. In these two equations, only the linear accelerations of the S/C are considered to emphasize the rotation-to-translation coupling of the S/C dynamics:

$$\vec{a}^{\,\mathrm{ST}} = \begin{bmatrix} a_x^{\mathrm{ST}} \\ a_y^{\mathrm{ST}} \\ a_z^{\mathrm{ST}} \end{bmatrix} = \begin{bmatrix} [\dot{\vec{\omega}} \times \overrightarrow{BH_1}] \cdot \hat{X} \\ 1/2[\dot{\vec{\omega}} \times (\overrightarrow{BH_1} + \overrightarrow{BH_2})] \cdot \hat{Y} \\ 1/2[\dot{\vec{\omega}} \times (\overrightarrow{BH_1} + \overrightarrow{BH_2})] \cdot \hat{Z} \end{bmatrix} \quad (10)$$

$$\vec{F}_{\mathrm{DF}}^{\,\mathrm{ST}} = \begin{bmatrix} F_{\mathrm{DF},x}^{\mathrm{ST}} \\ F_{\mathrm{DF},y}^{\mathrm{ST}} \\ F_{\mathrm{DF},z}^{\mathrm{ST}} \end{bmatrix} = -m_{S/C} \begin{bmatrix} a_x^{\mathrm{ST}} \\ a_y^{\mathrm{ST}} \\ a_z^{\mathrm{ST}} \end{bmatrix}. \quad (11)$$

The SSM predicts the influence of the star tracker, if set with a S/C center of mass located off the axis joining the two TMs. The set values in the model are the ones shown in Eq. (9). Figure 10 shows the impact of the ST noise on the S/C stability along the X-axis, together with all the other contributors already discussed in Sec. VIII. The solid blue trace is the combination of data sensor outputs given by Eqs. (12) and (13), and involving the double derivative of TM1 interferometer readout $\ddot{o}_1$ and the measurement of the force applied to the S/C along X to counteract the Euler force, presented in Eq. (11). The angular acceleration of the satellite needed to compute the Euler force amplitude is recovered from GRS θ_1 measurements, and z and y

differential measurements are differentiated twice and corrected from the direct electrostatic actuation applied to the TMs $T_X^{\rm cmd}$, $F_z^{\rm cmd}$, and $F_y^{\rm cmd}$ in order to trigger the S/C rotation according to the DFACS control scheme (see Table I):

$$a_X^{\rm S/C,meas} = -\ddot{o}_1 + [\dot{\vec{\omega}}^{\rm meas} \times B\vec{H}_1] \cdot \hat{X} \tag{12}$$

$$\dot{\vec{\omega}}^{\rm meas} = \begin{bmatrix} \frac{T_X^{\rm cmd}}{I_{XX}} - \ddot{\theta}_1 \\ \frac{F_{z2}^{\rm cmd}/m_2 - F_{z1}^{\rm cmd}/m_1}{H_1 H_2} - \frac{(\ddot{z}_2 - \ddot{z}_1)}{H_1 H_2} \\ \frac{F_{y2}^{\rm cmd}/m_2 - F_{y1}^{\rm cmd}/m_1}{H_1 H_2} - \frac{(\ddot{y}_2 - \ddot{y}_1)}{H_1 H_2} \end{bmatrix}. \tag{13}$$

Figure 10 shows solid agreement between SSM predictions and computations from observations of the influence of the star tracker noise on stability along the X-axis. It is visible in this figure that the star tracker noise significantly worsens platform stability at low frequencies by up to 3 orders of magnitude at 0.1 mHz. It is particularly noteworthy along the X-axis where high sensitivity of the optical sensor should have allowed for stability of the platform at the same level of quietness as the test mass itself (see the light green dashed line in Fig. 10), if it were not for the presence of a noisy sensor such as the star tracker (relative to the other sensors of very high performance) within the DFACS loop. It is also worth noting that the decrease of the stability performance due to S/C attitude sensing noise will be largely mitigated in the case of LISA, where differential wavefront sensing of the interspacecraft laser link will provide attitude measurement of much higher precision. Figure 10 shows a projection to LISA performances (light gray) following this consideration, hence excluding the contribution from the star tracker noise. Besides, in the case of LISA, studying the stability of the S/C center of mass is less relevant than studying the stability of the optical benches, which are geometrically much closer to the TMs, and thus less affected by the rotation-to-translation coupling discussed here.

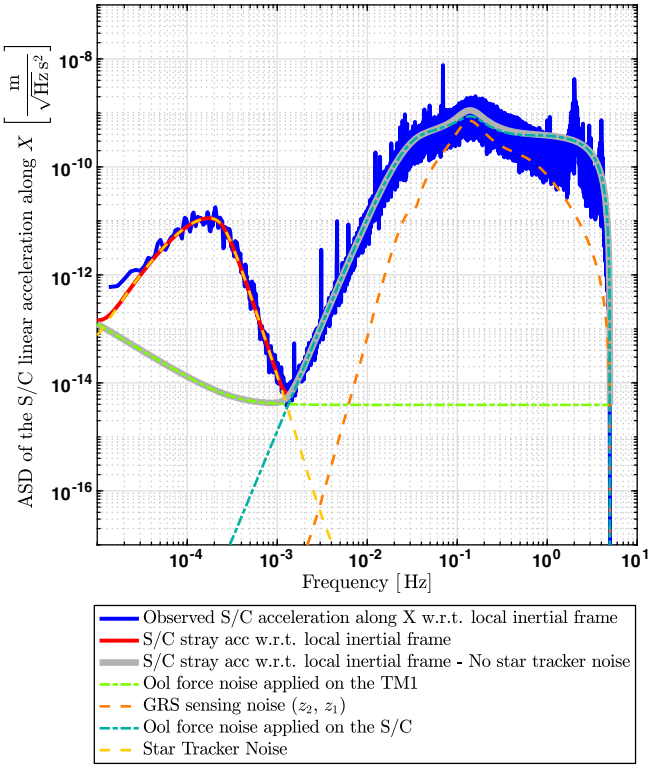

FIG. 10. Stability of the S/C along X as a function of frequency as simulated by the LPF ssm (red) and as measured with a combination of observed data (solid blue) that takes into account the impact of the star tracker noise [according to Eqs. (10) and (11)]. Similar to the red line, the gray solid trace gives the model prediction for X stability of the S/C, though excluding the impact of the star tracker, hence providing a projection to the LISA observatory case (for which attitude control will be driven by the DWS of the interspacecraft laser beam, seen as an inertial attitude reference). The dashed-line traces show the model decomposition. This figure uses parameters and data obtained from the April 2016 noise-only run.

X. CONCLUSION

A frequency domain analysis and a decomposition of all in-loop coordinates associated to TM1 has been presented in order to highlight the DFACS performance of the LPF mission. The stability of the LPF platform, with respect to a local geodesic, has also been estimated.

A number of points can be concluded from this study:

(i) The study has shown that the LPF platform has remarkable performance in terms of stability over all d.o.f. The privileged X-axis has outstanding performance, and the other d.o.f. also show remarkable performance which demonstrate the interest of such a platform for other applications. Improvements in some of the sensors and actuators could enhance this performance.

(ii) This study shows that the stability of LPF, in terms of acceleration with respect to the local inertial reference frame, is sensitive to the GRS sensing noise around 1 mHz and to the TM force noise at lower frequency. Above 0.1 Hz, the stability performances are impacted by the (microthruster) force noise and by the DFACS control loop.

(iii) Below 1 mHz, the noise of the star tracker strongly impacts the performance of the system on all d.o.f. It should be noted however that, for LISA, several orders of magnitude improvements on attitude control performances are expected, benefiting from 10^{-8} rad Hz$^{-1/2}$ precision attitude sensing with differential wavefront sensing on the incoming long-range laser beam [11], rather than the (10^{-4} rad Hz$^{-1/2}$) level achieved by the LPF star tracker at low frequency, around 0.1 mHz.

(iv) The SSM [25] developed by the LPF Collaboration provides a reliable description of the closed-loop

dynamics, showing that the LPF system can be approximated by a linear system for frequencies lower than 0.2 Hz. Hence, the SSM has been used to estimate the stability of the LPF platform over a wide frequency range, highlighting its remarkable performance.

(v) The demonstrated reliability of the model is an item of interest for the upcoming task of extrapolating LPF results towards LISA simulations and design. Such work is ongoing and will be published in the near future.

(vi) The quality of the performance obtained by the LPF platform, with respect to the local geodesic, should therefore allow definition of similar platforms for other types of space-based measurements.

ACKNOWLEDGMENTS

This work has been made possible by the LISA Pathfinder mission, which is part of the space-science program of the European Space Agency. The French contribution has been supported by the CNES (Accord spécifique de projet CNES 1316634/CNRS 103747), the CNRS, the Observatoire de Paris and the University Paris-Diderot. E. P. and H. I. would also like to acknowledge the financial support of the UnivEarthS Labex program at Sorbonne Paris Cité (Grants No. ANR-10-LABX-0023 and No. ANR-11-IDEX-0005-02). The Albert-Einstein-Institut acknowledges the support of the German Space Agency, DLR. The work is supported by the Federal Ministry for Economic Affairs and Energy based on a resolution of the German Bundestag (Grants No. FKZ 50OQ0501 and No. FKZ 50OQ1601). The Italian contribution has been supported by Agenzia Spaziale Italiana and Istituto Nazionale di Fisica Nucleare. The Spanish contribution has been supported by Contracts No. AYA2010-15709 (MICINN), No. ESP2013-47637-P, and No. ESP2015-67234-P (MINECO). M. N. acknowledges support from Fundacion General CSIC (Programa ComFuturo). F. R. acknowledges a FPI contract (MINECO). The Swiss contribution acknowledges the support of the Swiss Space Office (SSO) via the PRODEX Programme of ESA. L. F. is supported by the Swiss National Science Foundation. The U.K. groups wish to acknowledge support from the United Kingdom Space Agency (UKSA), the University of Glasgow, the University of Birmingham, Imperial College, and the Scottish Universities Physics Alliance (SUPA). J. I. T. and J. S. acknowledge the support of the U.S. National Aeronautics and Space Administration (NASA).

[1] B. D. Tapley, S. Bettadpur, M. Watkins, and C. Reigber, The gravity recovery and climate experiment: Mission overview and early results, Geophys. Res. Lett. **31**, L09607 (2004).

[2] D. Muzi and A. Allasio, GOCE: The first core Earth explorer of ESA's Earth observation programme, Acta Astron. **54**, 167 (2004).

[3] C. W. F. Everitt, D. B. DeBra, B. W. Parkinson *et al.*, Gravity Probe B: Final Results of a Space Experiment to Test General Relativity, Phys. Rev. Lett. **106**, 221101 (2011).

[4] P. Touboul, G. Métris, M. Rodrigues *et al.*, MICROSCOPE Mission: First Results of a Space Test of the Equivalence Principle, Phys. Rev. Lett. **119**, 231101 (2017).

[5] A. G. A. Brown, A. Vallenari, T. Prusti *et al.*, Gaia data release 1: Summary of the astrometric, photometric, and survey properties, Astron. Astrophys. **595**, A2 (2016).

[6] P. Chapman, T. Colegrove, E. Ecale, and B. Girouart, Gaia attitude control design: Milli-arcsecond relative pointing performance using micro-thrusters and instrument in the loop, *8th International ESA Conference on Guidance and Navigation Control, At Karlovy Vary, Czech Republic*, https://www.researchgate.net/publication/261710225_Gaia_Attitude_Control_Design_Milli-Arcsecond_Relative_Pointing_Performance_using_Micro-Thrusters_and_Instrument_in_the_Loop.

[7] S. Anza, M. Armano, E. Balaguer *et al.*, The LTP experiment on the LISA Pathfinder mission, Classical Quantum Gravity **22**, S125 (2005).

[8] M. Armano, H. Audley, G. Auger *et al.*, Sub-Femto-g Free Fall for Space-Based Gravitational Wave Observatories: LISA Pathfinder Results, Phys. Rev. Lett. **116**, 231101 (2016).

[9] M. Armano, H. Audley, G. Auger *et al.*, Beyond the Required Lisa Free-Fall Performance: New Lisa Pathfinder Results Down to 20 μHz, Phys. Rev. Lett. **120**, 061101 (2018).

[10] P. McNamara, S. Vitale, and K. Danzmann (LISA Pathfinder Collaboration), LISA Pathfinder, Classical Quantum Gravity **25**, 114034 (2008).

[11] P. Amaro-Seoane, H. Audley, S. Babak *et al.*, Laser interferometer space antenna, arXiv:1702.00786.

[12] R. Dolesi, D. Bortoluzzi, P. Bosetti *et al.*, Gravitational sensor for LISA and its technology demonstration mission, Classical Quantum Gravity **20**, S99 (2003).

[13] M. Armano, H. Audley, G. Auger *et al.*, Capacitive sensing of test mass motion with nanometer precision over millimeter-wide sensing gaps for space-borne gravitational reference sensors, Phys. Rev. D **96**, 062004 (2017).

[14] LISA Pathfinder Collaboration, Article dedicated to the measured noise performance of the LISA Pathfinder electrostatic actuation system (to be published).

[15] G. Heinzel, C. Braxmaier, R. Schilling, A. Rüdiger, D. Robertson, M. te Plate, V. Wand, K. Arai, U. Johann, and K. Danzmann, Interferometry for the LISA technology package (LTP) aboard SMART-2, Classical Quantum Gravity **20**, S153 (2003).

[16] G. Heinzel, V. Wand, A. García *et al.*, The LTP interferometer and phasemeter, Classical Quantum Gravity **21**, S581 (2004).
[17] H. Audley, K. Danzmann, A. G. Marn *et al.*, The LISA Pathfinder interferometry—hardware and system testing, Classical Quantum Gravity **28**, 094003 (2011).
[18] G. Anderson, J. Anderson, M. Anderson *et al.*, Experimental results from the ST7 mission on LISA Pathfinder, Phys. Rev. D **98**, 102005 (2018).
[19] W. Fichter, P. Gath, S. Vitale, and D. Bortoluzzi, LISA Pathfinder drag-free control and system implications, Classical Quantum Gravity **22**, S139 (2005).
[20] A. Schleicher, T. Ziegler, R. Schubert *et al.*, In-orbit performance of the LISA Pathfinder drag-free and attitude control system, CEAS Space J. **10**, 471 (2018).
[21] General space dynamics and control strategy consisting of a spacecraft enclosing a reference of inertia (test mass) protected from the environmental disturbances and w.r.t. which the S/C locks its dynamics, hence counterbalancing external forces such as the drag of the atmosphere, thus allowing for a quasi inertial movement of the S/C.
[22] The control loop mode when the science measurements were performed. Table I details the control scheme for this mode.
[23] P. Welch, The use of fast Fourier transform for the estimation of power spectra: A method based on time averaging over short, modified periodograms, IEEE Trans. Audio Electroacoust. **15**, 70 (1967).
[24] S. Vitale, G. Congedo, R. Dolesi *et al.*, Data series subtraction with unknown and unmodeled background noise, Phys. Rev. D **90**, 042003 (2014).
[25] M. Weyrich and A. Grynagier, The SSM class: modelling and analyses for the LISA Pathfinder technology experiment, Institut für Flugmechanik und Flugregelung, Universität Stuttgart Technical Report No. S2-iFR-TN-3003, 2008.
[26] M. Hewitson, M. Armano, M. Benedetti *et al.*, Data analysis for the LISA technology package, Classical Quantum Gravity **26**, 094003 (2009).
[27] LISA Pathfinder Collaboration, LISA Pathfinder closed-loop analysis: A model breakdown of the in-loop observables, J. Phys. Conf. Ser. **840**, 012038 (2017).
[28] Our writing convention uses upper case for dynamic variables regarding the S/C, and lower cases for those regarding the TMs.

Correction: Figure 8 was presented with two minor errors in an axis label and key description and has been fixed.